

# Comparison of the calorimetric and kinematic methods of neutrino energy reconstruction in disappearance experiments

A. M. Ankowski,<sup>1,\*</sup> O. Benhar,<sup>2,1</sup> P. Coloma,<sup>3</sup> P. Huber,<sup>1</sup> C.-M. Jen,<sup>1</sup> C. Mariani,<sup>1</sup> D. Meloni,<sup>4</sup> and E. Vagnoni<sup>4</sup>

<sup>1</sup>*Center for Neutrino Physics, Virginia Tech, Blacksburg, Virginia 24061, USA*

<sup>2</sup>*INFN and Department of Physics, “Sapienza” Università di Roma, I-00185 Roma, Italy*

<sup>3</sup>*Fermi National Accelerator Laboratory, Batavia, Illinois 60510, USA*

<sup>4</sup>*INFN and Dipartimento di Matematica e Fisica,  
 Università di Roma Tre, Via della Vasca Navale 84, 00146 Rome, Italy*

To be able to achieve their physics goals, future neutrino-oscillation experiments will need to reconstruct the neutrino energy with very high accuracy. In this work, we analyze how the energy reconstruction may be affected by realistic detection capabilities, such as energy resolutions, efficiencies, and thresholds. This allows us to estimate how well the detector performance needs to be determined *a priori* in order to avoid a sizable bias in the measurement of the relevant oscillation parameters. We compare the kinematic and calorimetric methods of energy reconstruction in the context of two  $\nu_\mu \rightarrow \nu_\mu$  disappearance experiments operating in different energy regimes. For the calorimetric reconstruction method, we find that the detector performance has to be estimated with a  $\mathcal{O}(10\%)$  accuracy to avoid a significant bias in the extracted oscillation parameters. On the other hand, in the case of kinematic energy reconstruction, we observe that the results exhibit less sensitivity to an overestimation of the detector capabilities.

PACS numbers: 14.60.Pq, 14.60.Lm, 13.15.+g, 25.30.Pt

## I. INTRODUCTION

Long-baseline experimental searches of neutrino oscillations largely rely on the capability of pinning down the energy dependence of the oscillation probability, which is a nontrivial function of the *true* neutrino energy,  $E_\nu$ . As a consequence, the procedure employed to reconstruct the unknown incoming-neutrino energy from the measured kinematics of the interaction products is a central element of the oscillation analysis.

Experiments using neutrino beams peaked at  $E_\nu \sim 600\text{--}800$  MeV, such as T2K [1] and MiniBooNE [2], determine the energy distribution of charged current (CC) events from the kinematics of the outgoing current lepton—i.e., its kinetic energy and emission angle—measured by large Cherenkov detectors filled with water or mineral oil. This technique is mostly applied to quasielastic (QE) events—identified by the absence of pions in the final state—that provide the dominant contribution to the total cross section at these energies. However, it necessarily involves hypotheses on the reaction mechanism.

The kinematic method of energy reconstruction is based on the assumptions that the beam particle interacts with a single nucleon at rest, bound with constant energy, and that no other nucleons are knocked out from the nucleus. It is long known, however, that processes involving two-nucleon currents, final-state interactions, and nucleon-nucleon correlations give rise to the appearance of more complex final states, featuring more than one nucleon excited to the continuum. Reconstruction

of the neutrino energy of such events, dubbed QE-like in the mesonless case [3], in general requires more complex methods, involving realistic models of nuclear dynamics.

At energies well above 1 GeV, the contribution of inelastic processes—resonance production and deep-inelastic scattering (DIS)—becomes larger and eventually dominant. In this case, the determination of the neutrino energy requires reconstruction of events with many hadrons, both nucleons and mesons, in the final state.

As alternative to Cherenkov detectors in this regime, calorimeters measuring the visible energy associated with each event—i.e., the energy deposited by the final-state particles—have been proposed as effective devices, allowing for an accurate neutrino-energy reconstruction. For example, calorimeters are presently being used in the MINOS [4] and NO $\nu$ A [5] experiments. In their detectors, the total energy deposited by all reaction products is measured without a prior reconstruction of each final-state particle’s track, momentum or energy. The energy response for potentially complex final states is calibrated using test-beam exposures. On the other hand, future appearance experiments like DUNE [6] are expected to employ detectors capable of fine-grained tracking of a large number of interaction products. In their case, the tracking capability is the key to be able to select electron-neutrino events and distinguish them from backgrounds, even for non-QE events.

In this article, we compare the kinematic and calorimetric reconstruction methods in the oscillation analysis of a  $\nu_\mu$  disappearance experiment. We also aim to explore the capabilities and limitations of a calorimetric analysis based on individually identified particle tracks, and to determine what level of understanding of detector response and underlying events is required to meet certain

\* ankowski@vt.edu

physics goals.

For a muon-neutrino event, it is clear that the long muon track in itself is a clear signature and no tracking beyond the leading muon is required for backgrounds removal. However, we study the  $\nu_\mu$  disappearance channel because of its simplicity in terms of oscillation physics and as a sandbox to develop suitable analysis tools.

The calorimetric technique as defined above obviously rests on the ability of fully reconstructing the final state, which largely depends on the detector design and performance. Nuclear effects also play a role, as they may lead to a sizeable amount of *missing* energy, hindering the reconstruction of  $E_\nu$ . For example, if a pion produced at the elementary interaction vertex is absorbed in the spectator system, in general, its energy is not deposited in the calorimeter.

We consider an idealized setting, in which the near and far detectors are functionally identical, and a simple extrapolation between them can be performed [7]. To minimize the uncertainty arising from nuclear interactions, the target nucleus selected for both detectors is carbon, the cross section of which has been extensively measured in a number of different channels [8–28].

The analyzed events are generated using the simulation code GENIE [29] supplemented with the  $\nu T$  package of additional modules [30], allowing to describe the carbon ground state using the realistic spectral function [31].

In order to cover different experimental configurations, we consider two options: a low-energy (LE) setup, with a narrow-band off-axis beam, and a high-energy (HE) setup, featuring a broad-band on-axis beam. In the LE option, the neutrino flux is peaked around 600 MeV and the distance to the far detector is set to  $L = 295$  km, while in the HE option, the flux is peaked at  $\sim 1$ – $2$  GeV and  $L = 1000$  km.

Event reconstruction is carried out assuming

- (i) a *perfect* scenario, in which all produced particles are detected and their true energies are measured,
- (ii) a *realistic* one, in which detection efficiencies and thresholds are taken into account, and the finite detector resolution leads to a smearing of the measured energies.

In both cases, neutrons are assumed to escape detection altogether.

A key element of our analysis are the migration matrices, the elements of which,  $\mathcal{M}_{ij}$ , correspond to the probability that an event with a true neutrino energy in the  $j$ th bin ends up being reconstructed in an energy bin  $i$ .

The event distribution representing the data is in each case generated using the realistic scenario. Fitted rates, on the other hand, are obtained using a linear combination of migration matrices corresponding to the perfect and realistic scenarios. This procedure is very effective from the computational point of view, and provides a measure of the impact of detector performance on the oscillation-parameters fit.

This article is structured as follows. In Sec. II we derive different methods of neutrino-energy reconstruction, placing a special emphasis on the approximations involved. The neutrino cross-section model employed for event generation and the treatment of detector effects are outlined in Secs. III and IV, respectively. In Sec. V we discuss the calculated migration matrices. Our oscillation analysis and its results are presented in Sec. VI. Finally, in Sec. VII we summarize our findings.

## II. ENERGY RECONSTRUCTION METHODS

Consider CC neutrino scattering off a nuclear target, resulting in the knockout of  $n$  nucleons and production of  $m$  mesons. The energy and momentum conservation can be cast in the form

$$E_\nu + M_A = E_\ell + E_{A-n} + \sum_i E_{\mathbf{p}'_i} + \sum_j E_{\mathbf{h}'_j}, \quad (1)$$

$$\mathbf{k}_\nu = \mathbf{k}_\ell - \mathbf{p} + \sum_i \mathbf{p}'_i + \sum_j \mathbf{h}'_j, \quad (2)$$

respectively, where  $E_\nu$  and  $\mathbf{k}_\nu$  ( $E_\ell$  and  $\mathbf{k}_\ell$ ) are the neutrino's (charged lepton's) energy and momentum,  $E_{\mathbf{p}'_i}$  and  $\mathbf{p}'_i$  denote the energy and momentum of the  $i$ th knocked-out nucleon ( $1 \leq i \leq n$ ), and  $E_{\mathbf{h}'_j}$  and  $\mathbf{h}'_j$  stand for the energy and momentum of the  $j$ th produced meson ( $1 \leq j \leq m$ ). The energy of the residual ( $A - n$ )-nucleon system,  $E_{A-n}$ , can be conveniently expressed as

$$E_{A-n} = M_A - nM + E + T_{A-n}, \quad (3)$$

in terms of the nucleon (target nucleus) mass  $M$  ( $M_A$ ), the recoil energy  $T_{A-n}$ , and the excitation energy  $E$ . In Eq. (2), the recoil momentum of the system is denoted as  $-\mathbf{p}$ , to allow the interpretation of  $\mathbf{p}$  as the vector sum of the initial momenta of the knocked-out nucleons, assuming that it is not altered by final-state interactions with the residual system.

Substitution of Eq. (3) into Eq. (1) leads to the neutrino energy in the form

$$E_\nu = E_\ell + E + T_{A-n} + \sum_i (E_{\mathbf{p}'_i} - M) + \sum_j E_{\mathbf{h}'_j}. \quad (4)$$

Note that, while for mesons the total energies enter the sum, for nucleons only the kinetic energies contribute. This difference is a consequence of the fact that mesons are produced in the interaction process, whereas nucleons are only knocked out from the target nucleus.

Assuming that multinucleon effects do not introduce strong energy-dependence to the cross sections, the factor  $\epsilon_n = E + T_{A-n}$  can be treated as a constant at neutrino energies above several hundred MeV. Then, reconstruction of the neutrino energy reduces to determining the energies of the particles in the final state [32],

$$E_\nu^{\text{cal}} = \epsilon_n + E_\ell + \sum_i (E_{\mathbf{p}'_i} - M) + \sum_j E_{\mathbf{h}'_j}. \quad (5)$$

This, so-called, calorimetric method can, in principle, be applied to any type of CC interaction. However, one needs to keep in mind that an accurate reconstruction of hadrons poses a formidable experimental challenge. In particular, neutrons typically escape detection, and any undetected meson results in energy underestimation by at least the value of the pion mass,  $\sim 135$  MeV.

When the invariant hadronic mass squared, defined as

$$W^2 = \left( \sum_i E_{\mathbf{p}'_i} + \sum_j E_{\mathbf{h}'_j} \right)^2 - \left( \sum_i \mathbf{p}'_i + \sum_j \mathbf{h}'_j \right)^2,$$

is known, Eqs. (1) and (2) can be solved for the neutrino energy, yielding the alternative expression [33]

$$E_\nu = \frac{2E_{\mathbf{p}}E_\ell - 2\mathbf{p} \cdot \mathbf{k}_\ell + W^2 - (E_{\mathbf{p}}^2 - \mathbf{p}^2) - m_\ell^2}{2(E_{\mathbf{p}} - |\mathbf{p}| \cos \theta_N - E_\ell + |\mathbf{k}_\ell| \cos \theta)}, \quad (6)$$

where  $E_{\mathbf{p}} = M_A - E_{A-n}$ ,  $m_\ell$  is the charged lepton's mass,  $|\mathbf{p}| \cos \theta_N = \mathbf{p} \cdot \mathbf{k}_\nu / E_\nu$ , and  $|\mathbf{k}_\ell| \cos \theta = \mathbf{k}_\ell \cdot \mathbf{k}_\nu / E_\nu$ .

On the other hand, in the case of a single-nucleon knockout associated with production of  $m$  mesons, the requirement that the nucleon is on the mass shell,  $E_{\mathbf{p}'}^2 = M^2 + \mathbf{p}'^2$ , can be used to obtain the neutrino energy as

$$E_\nu = \frac{M^2 + (\mathbf{p} - \mathbf{k}_\ell - \sum_j \mathbf{h}'_j)^2 - (E_{\mathbf{p}} - E_\ell - \sum_j E_{\mathbf{h}'_j})^2}{2[E_{\mathbf{p}} - |\mathbf{p}| \cos \theta_N - E_\ell + |\mathbf{k}_\ell| \cos \theta - \sum_j \mathcal{H}_j]}, \quad (7)$$

with  $\mathcal{H}_j = E_{\mathbf{h}'_j} - \mathbf{h}'_j \cdot \mathbf{k}_\nu / E_\nu$ .

In practice, an application of the above formulas requires (i) neglecting the unmeasured recoil momentum  $|\mathbf{p}|$  and (ii) approximating the energy of the residual nuclear system by a constant, which amounts to setting  $E_{\mathbf{p}'} = nM - \epsilon_n$  in Eq. (6) and  $E_{\mathbf{p}} = M - \epsilon$  in Eq. (7). These simplifications lead to the expressions

$$E_\nu^{\text{kin}} = \frac{2(nM - \epsilon_n)E_\ell + W^2 - (nM - \epsilon_n)^2 - m_\ell^2}{2(nM - \epsilon_n - E_\ell + |\mathbf{k}_\ell| \cos \theta)}, \quad (8)$$

and

$$E_\nu^{\text{mt}} = \frac{M^2 + (\mathbf{k}_\ell + \sum_j \mathbf{h}'_j)^2 - (M - \epsilon - E_\ell - \sum_j E_{\mathbf{h}'_j})^2}{2(M - \epsilon - E_\ell + |\mathbf{k}_\ell| \cos \theta - \sum_j \mathcal{H}_j)}. \quad (9)$$

Owing to difficulties with an accurate determination of the invariant hadronic mass, the use of Eq. (8) is usually restricted to the process of single-nucleon knockout with no pions produced, in which  $W^2$  is known and equals  $M^2$  [9, 14, 15, 34, 35]. On the other hand, Eq. (9) has been applied in energy reconstruction for single-pion events by the MiniBooNE Collaboration [12], setting the single-nucleon separation energy  $\epsilon$  to zero.

The kinematic energy reconstruction, by means of Eqs. (8) or (9), does not require the knocked-out nucleon's momentum to be measured. However, as this method assumes specific final states, its accuracy is spoiled by any undetected hadron. For example, when a produced pion is absorbed or undetected, the energy

reconstructed from Eq. (8) under the QE hypothesis is typically lower than the true one by  $\sim 300$ – $350$  MeV, see Figs. 6 and 7 of Ref. [36]. While the process of multi-nucleon knockout affects the energy reconstruction in a similar way—i.e., it redistributes the strength of the reconstructed flux from the peak mainly to the low-energy tail [37, 38]—this effect seems to be less relevant at higher beam energies [39].

For completeness, we mention that neutrino energy can be also found exploiting momentum conservation only. Equation (2) multiplied by a factor  $\mathbf{k}_\nu / E_\nu$ ,

$$E_\nu = |\mathbf{k}_\ell| \cos \theta - |\mathbf{p}| \cos \theta_N + \sum_i |\mathbf{p}'_i| \cos \theta_i + \sum_j |\mathbf{h}'_j| \cos \theta_j, \quad (10)$$

where  $|\mathbf{p}'_i| \cos \theta_i = \mathbf{p}'_i \cdot \mathbf{k}_\nu / E_\nu$  and  $|\mathbf{h}'_j| \cos \theta_j = \mathbf{h}'_j \cdot \mathbf{k}_\nu / E_\nu$ , shows that  $E_\nu$  can be determined from the projections of the final momenta on the beam direction. Neglecting the contribution of the recoil momentum, one obtains the expression

$$E_\nu^{\text{mom}} = |\mathbf{k}_\ell| \cos \theta + \sum_i |\mathbf{p}'_i| \cos \theta_i + \sum_j |\mathbf{h}'_j| \cos \theta_j, \quad (11)$$

a special case of which has been employed in analysis of single-nucleon knockout events by the NOMAD Collaboration [9].

Performing the kinematic energy reconstruction in this article, we employ Eq. (8) assuming single-nucleon knockout, regardless of the actual number of nucleons in the final state. We set  $W^2$  to  $M^2$  for mesonless events and to  $M_\Delta^2$ ,  $M_\Delta = 1.232$  GeV being the  $\Delta$  resonance mass, when at least one meson is *observed*. The single-nucleon separation energy is fixed to 34 MeV. The same value of  $\epsilon$  is added in the calorimetric energy reconstruction (5) for every nucleon detected.

### III. EVENT GENERATION

Our analysis is based on the description of nuclear structure and interaction dynamics in the GENIE Monte Carlo generator [29], version 2.8.0, supplemented with the  $\nu T$  package of additional modules [30].

GENIE is a modern and versatile platform for neutrino event simulation. Due to the importance for ongoing and future oscillation studies, it has been developed putting special emphasis on scattering in the energy region of few GeV, where various mechanism of interaction are relevant. A number of neutrino experiments employs this generator in data analysis [40].

Resonant pion production in GENIE, considered for  $W \leq 1.7$  GeV, is accounted for using the model of Rein and Sehgal [41]. Compared to 18 in the original model, 16 resonances of unambiguous existence are implemented using up-to-date parameters but neglecting interference between them. The effect of the charged lepton's mass is taken into account only in calculations of the phase-space boundaries.

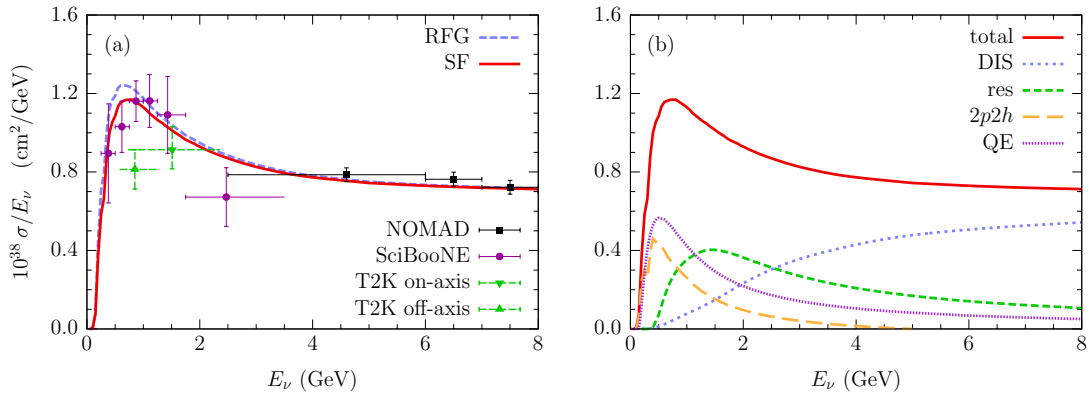


FIG. 1. (color online). Panel (a): Per-nucleon CC inclusive  $\nu_\mu$  cross section divided by neutrino energy, obtained using GENIE 2.8.0+ $\nu T$  [29, 30] with the relativistic Fermi gas model (dashed line) and the spectral function approach (solid line) as a nuclear model in QE interaction. The results for carbon are compared to the experimental data for the carbon, polystyrene ( $C_8H_8$ ), and hydrocarbon (CH) targets reported by the NOMAD [8], SciBooNE [14], and T2K [17, 19] Collaborations, respectively. Panel (b): Breakup of the contributions to the inclusive cross section. The labels DIS, res,  $2p2h$ , and QE refer to deep-inelastic scattering, resonant pion production, two-nucleon knockout, and quasielastic scattering, respectively.

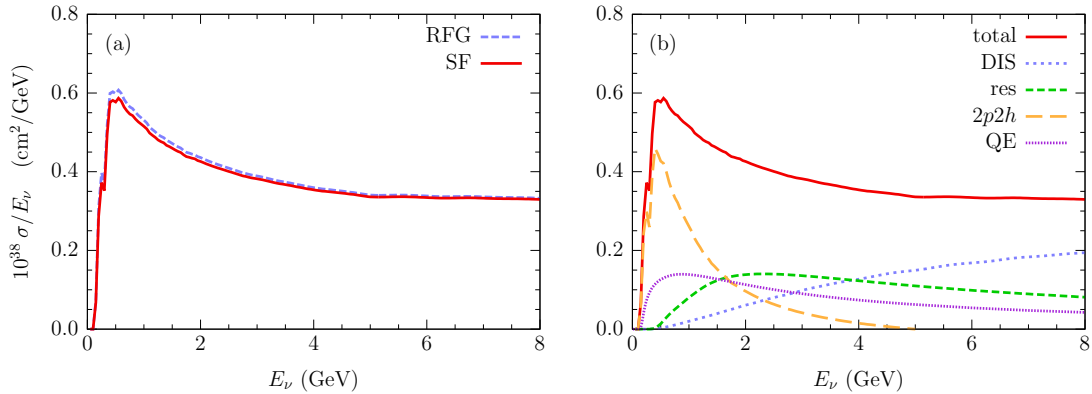


FIG. 2. (color online). Same as in Fig. 1 but for  $\bar{\nu}_\mu$ .

The contribution of nonresonant processes, classified in GENIE as DIS, is calculated following the method of Bodek and Yang [42, 43]. This effective approach extends the range of applicability of the parton model to low neutrino energy by modifying the (leading-order) parton-distribution functions in the low- $Q^2$  region,  $Q^2$  being the four-momentum transfer squared. Higher-order and target-mass corrections are accounted for by replacing Bjorken  $x$  with a new scaling variable [42, 43]. While DIS in GENIE is the only mechanism of interaction at  $W > 1.7$  GeV, it also produces one- and two-pion events in the resonance region.

Hadronization in GENIE is performed using the Andreopoulos-Gallagher-Kehayias-Yang approach [44], which combines Koba-Nielsen-Olesen (KNO) scaling [45] at low values of the hadronic invariant mass with the PYTHIA/JETSET calculations [46] at high  $W$ , ensuring smooth transition between the two regimes.

Two-nucleon knockout ( $2p2h$ ) events are simulated in GENIE using the procedure of Dytman [47], obtained modifying and extending the one of Ref. [48], derived for

electron scattering. The invariant mass of two-nucleon events is assumed to have a Gaussian distribution centered at  $W = (M + M_\Delta)/2$ . The charged lepton's kinematics is distributed according to the magnetic contribution to the cross section for scattering on a free nucleon [49], identical for neutrinos and antineutrinos. The strength, adjusted to fit the cross sections reported by MiniBooNE [10, 18], is implemented to linearly decrease to zero for the neutrino energy between 1 and 5 GeV, to avoid inconsistency with the results from NOMAD [9]. As the experimental data constrain the two-nucleon contribution for the carbon target only, for other nuclei, its strength is assumed to exhibit linear dependence on the mass number  $A$ .

In QE scattering, the default nuclear model in GENIE is the relativistic Fermi gas (RFG) model of Bodek and Ritchie [50], in which a high-momentum tail—inspired by the effects of nucleon-nucleon correlations—is added to the nucleon momentum distribution.

Using the  $\nu T$  package [30], we replace the RFG model by the spectral function (SF) approach [51], the imple-

mentation of which has been validated through comparisons with electron-scattering data. In the SF formalism, the interaction between the beam particle and the nucleus is assumed to involve a single nucleon, with the remaining  $(A - 1)$  nucleons acting as spectators. Under this assumption—called the impulse approximation—the target initial state can be described by the nuclear spectral function  $P(\mathbf{p}, E)$ , giving the probability distribution that removal of a nucleon with momentum  $\mathbf{p}$  from the nuclear ground state leaves the residual  $(A - 1)$ -nucleon system with excitation energy  $E$ .

The realistic SF of carbon, employed in the  $\nu T$  package, has been obtained by the authors of Ref. [31] in the local density approximation (LDA). The LDA scheme relies on the premise that surface and shell effects do not affect short-range correlations between nucleons in nuclei, and it is supported by the evidence that for  $|\mathbf{p}| \gtrsim 300$  MeV, the momentum distribution is largely independent of the mass number  $A$ , for nuclei with  $A \geq 4$  [51]. Therefore, using LDA, the correlation contribution to the nuclear SF can be obtained from theoretical calculations for uniform nuclear matter at different densities [31, 52], and consistently combined with the shell structure of the nucleus, deduced from experimental  $(e, e'p)$  data [53, 54]. We stress that the carbon SF of Ref. [31] has proven successful in describing electron scattering data in various kinematical setups, see e.g. Ref. [55], and the momentum distribution obtained from it is consistent with the one extracted from  $(e, e'p)$  data at large missing energy and momentum [56].

The effect of using the  $\nu T$  package on the total inclusive CC cross section for muon neutrinos in GENIE is presented in Fig. 1(a). On the one hand, the SF calculation of the QE cross section clearly improves the agreement with the experimental data reported by the SciBooNE Collaboration [14]. On the other hand, it does not alter the good agreement at the kinematics of the NOMAD experiment [8], where the inclusive cross section is dominated by the contributions of DIS processes and resonant pion production, see Fig. 1(b). Note that in the case of the NOMAD data, the error bars represent  $\Delta(\sigma/E_\nu)$ , whereas for the SciBooNE points, they correspond to  $(\Delta\sigma)/E_\nu$  [14].

While the calculations do not seem to reproduce the SciBooNE point at the average neutrino energy of 2.47 GeV, it is important to note that its energy range extends over the whole high-energy tail of the flux, and does not end at 3.5 GeV.

The recent results of the T2K experiment [17, 19] suggest that in the  $\sim 1$  GeV region, uncertainties of the inclusive cross section may be sizable, of the order of 20%, and that the contribution of the  $2p2h$  processes may be smaller than that deduced from MiniBooNE. Should the  $2p2h$  estimate be significantly reduced in GENIE, the calculated cross sections would be in very good agreement with the T2K data.

For the sake of completeness, in Fig. 2 we show the total inclusive CC cross section for muon antineutrinos, for

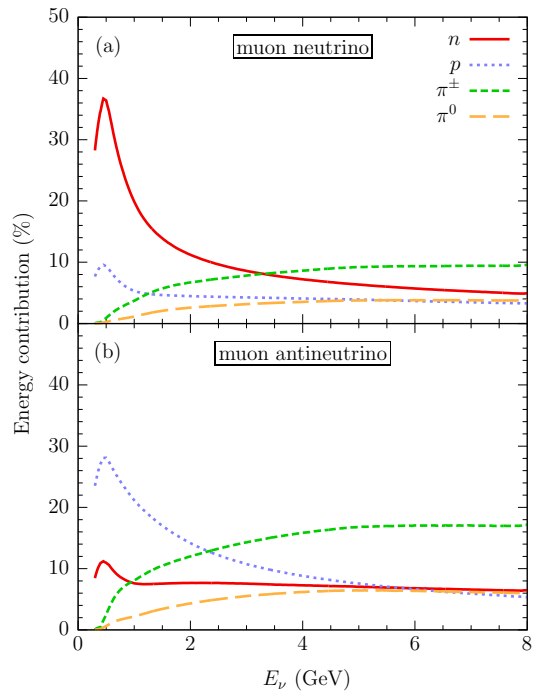


FIG. 3. (color online). Fraction of the (a)  $\bar{\nu}_\mu$  and (b)  $\nu_\mu$  energy converted into the kinetic energies of neutrons (solid lines) and protons (dotted lines), and the total energies of charged (short dashed lines) and neutral (long dashed lines) pions.

which experimental data are not available. It clearly appears that the  $2p2h$  contribution—which in GENIE [47] is assumed to be the same for neutrinos and antineutrinos—plays a much more important role in the latter case.

In the context of the calorimetric energy reconstruction, it is important to estimate how different species of hadrons contribute to the final-state energy. In Fig. 3 we present the obtained fraction of the  $\bar{\nu}_\mu$  and  $\nu_\mu$  energy carried out by neutrons, protons, and pions.

While at energies below  $\sim 1$  GeV, there is a clear difference between the neutron results for neutrinos and antineutrinos, it undergoes a sizeable reduction when DIS and resonant pion production become the dominant reaction mechanisms. Having in mind the numerical uncertainties—estimated not to exceed 1%—we conclude that at  $E_\nu \gtrsim 1.5$  GeV, neutrons contribute less than 15% of the (anti)neutrino energy.

As can be expected from QE interactions, the contribution of protons in antineutrino interactions resembles that of neutrons in neutrino scattering, and vice versa. For antineutrinos, the knocked-out protons carry out less than 10% of the initial energy in the whole considered region. However, for neutrinos, the protons contribution is much more sizable and reduces to  $\leq 10\%$  for energies exceeding  $\sim 3.35$  GeV.

Although the total energies of  $\pi^0$ 's enter the calorimetric energy reconstruction, in the considered kinematic range, their contributions are smaller than that of neu-

trons. On the other hand, in the region dominated by resonant and nonresonant pion production, charged pions give the largest contribution to the final-state hadronic energy.

We observe that at energies above 0.5 GeV, the analogical results for electron neutrinos and antineutrinos do not differ significantly from those presented in Fig. 3.

#### IV. CONSIDERED DETECTOR EFFECTS

In our analysis, two extreme sets of assumptions are considered regarding the detector performance:

(i) Perfect reconstruction.

With the exception of neutrons, all the produced particles are observed and their measured energies are equal to the true ones.

(ii) Realistic setup.

The measured energies and angles are smeared with respect to the true ones by finite detector resolution. The detection efficiencies and thresholds are taken into account. Neutrons are assumed to escape detection.

The detection thresholds applied in our calculations correspond to the measured kinetic energy of 20 MeV for mesons and 40 MeV for protons. For comparison, the NOMAD and MiniBooNE experiments were able to detect protons of kinetic energy above  $\sim 50$  MeV [9], and the  $\sim 40$ -MeV threshold is expected for future liquid-argon detectors [57].

The efficiencies are treated as energy-independent, for the sake of simplicity, and set to 60% for  $\pi^0$ 's, 80% for other mesons, and 50% for protons. Those values can be considered rather optimistic, compared to the efficiencies achieved in existing detectors [9, 58, 59]. We assume that produced charged leptons are always detected.

Accounting for the effect of finite detector resolution on an observable  $x_{\text{meas}}$ , we smear it according to the Gaussian distribution centered at the true value  $x_{\text{true}}$ ,

$$f(x_{\text{meas}}) = \frac{1}{\sqrt{2\pi}\sigma(x_{\text{true}})} \exp \left[ -\frac{1}{2} \left( \frac{x_{\text{meas}} - x_{\text{true}}}{\sigma(x_{\text{true}})} \right)^2 \right].$$

In the case of muon, we apply this procedure to the momentum and production angle, using

$$\sigma(|\mathbf{k}_\mu|) = 0.02|\mathbf{k}_\mu| \quad \text{and} \quad \sigma(\theta) = 0.7^\circ, \quad (12)$$

as in the MINERvA experiment [60]. For electron, the realistic resolutions [5, 61]

$$\sigma(E_e) = 0.10E_e \quad \text{and} \quad \sigma(\theta) = 2.8^\circ \quad (13)$$

are used.

For other particles, the only smeared quantity is the energy. To the electromagnetic showers produced by  $\pi^0$

decays, we employ the energy resolution given by

$$\frac{\sigma(E_{\pi^0})}{E_{\pi^0}} = \max \left\{ \frac{a_{\pi^0}}{\sqrt{E_{\pi^0}}}, \frac{b_{\pi^0}}{E_{\pi^0}} \right\} \quad (14)$$

with  $a_{\pi^0} = 0.107$ ,  $b_{\pi^0} = 0.02$ , while for other hadrons,

$$\frac{\sigma(E_h)}{E_h} = \max \left\{ \frac{a_h}{\sqrt{E_h}}, b_h \right\} \quad (15)$$

is used with  $a_h = 0.145$  and  $b_h = 0.067$ . The values of  $\sigma$  and the energies appearing in Eqs. (14) and (15) are expressed in units of GeV. Note that the hadron-energy resolutions applied in our analysis can be considered optimistic, as they are to be compared to

$$\frac{\sigma(E_{\pi^0})}{E_{\pi^0}} = 2\sqrt{\frac{a_{\pi^0}^2}{E_{\pi^0}} + \frac{b_{\pi^0}^2}{E_{\pi^0}^2}} \quad \text{and} \quad \frac{\sigma(E_h)}{E_h} = 2\sqrt{\frac{a_h^2}{E_h} + b_h^2}$$

achieved in the MINOS [4] and MINERvA [60] experiments. Note that the assumed  $\pi^+$  energy resolution is also optimistic when compared with the expectation for future liquid-argon detectors from Ref. [62].

It is important to emphasize that in the context of kinematic method of energy reconstruction, our assumptions are conservative. We employ realistic detector resolutions for muons and make minimal use of information on observed hadrons. Disregarding additional protons in the final state, we reconstruct every event as if it involved single-nucleon knockout. All mesons in the final state are assumed to originate from a single resonance of invariant mass  $M_\Delta = 1.232$  GeV, and their angular distributions are not taken into account, compare to Eq. (9). On the other hand, detector effects entering the calorimetric method are treated in an optimistic way, compared to those in existing detectors.

#### V. MIGRATION MATRICES

In a neutrino-oscillation experiment, detection efficiencies, thresholds, and energy resolutions for different particles affect the probability for a neutrino event to be reconstructed in the correct energy bin. In an ideal detector such probability would be a delta-function centered at the true neutrino energy. As the detector capabilities are reduced with respect to the ideal case, the probability distribution will get broader. If there is a significant energy carried away by particles missed by the detector, the mean of the distribution may drift away from the true neutrino energy as well and become asymmetric, with a longer tail extending to lower energies.

A few examples for such probability distributions are shown in Fig. 4, for two different types of neutrino interactions and two different values of the neutrino energy. The probability is shown as a function of the reconstructed energy, for the “perfect” and “realistic” scenarios described in Sec. IV. For reference, the results

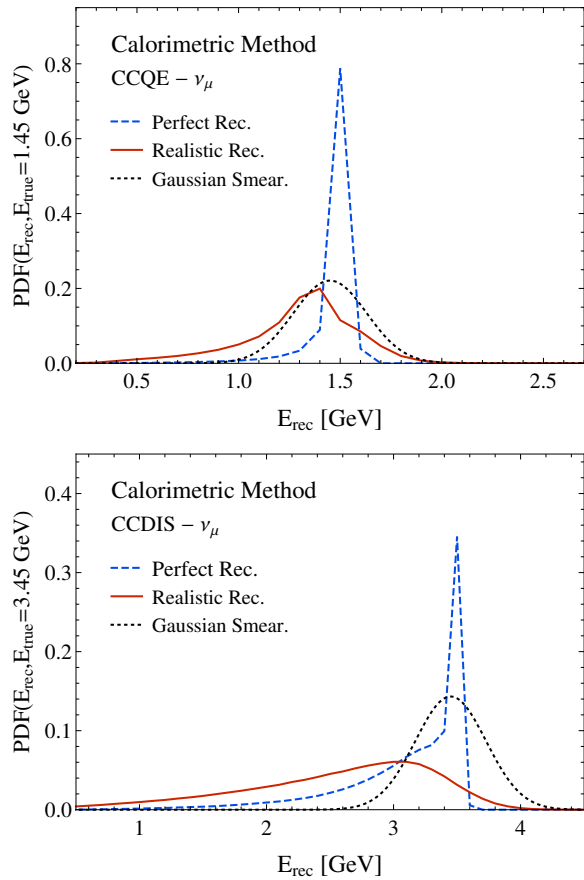


FIG. 4. (color online). Probability distribution functions for a neutrino event of the true energy  $E_{\text{true}}$  to be reconstructed at the energy  $E_{\text{rec}}$ . Results are shown for QE neutrino event at  $E_{\text{true}} = 1.45$  GeV (top) and a DIS event at  $E_{\text{true}} = 3.45$  GeV (bottom), as well as for different assumptions on the detector performance, see text for details.

using a detector with effective smearing in neutrino energy according to a Gaussian with standard deviation  $\sigma(E_\nu) = 0.15\sqrt{E_\nu}$  centered is also shown. Note that such resolution is typically assumed in phenomenological studies devoted to liquid-argon detectors [57, 63–66].

The probability for a neutrino event to be reconstructed at a particular neutrino energy obviously depends on the reconstruction procedure, as well as on the event type. In Fig. 4 we show two examples for the calorimetric energy reconstruction, for QE and DIS events. The reconstruction works rather well for a QE neutrino event, and the probability to get the energy reconstructed at a very different value other than the true neutrino energy is relatively small. For a DIS event, on the other hand, the probability is rather flat, and there is a clear tendency to get the energy reconstructed at lower values than the true one. This is mostly due to the role played by neutrons—assumed to be undetected—and other particles unobserved due to the realistic detection efficiencies and thresholds.

The probability distribution functions (PDF) described above and presented in Fig. 4 can be used to compute the columns in a migration matrix (one for each possible true value of the neutrino energy). The observed event sample at the detector can then be computed as

$$N_i^{\text{tot}} = \sum_X \sum_j \mathcal{M}_{ij}^X N_j^X,$$

where  $X$  runs over the four types of interactions considered (DIS, res, 2p2h, and QE),  $i$  and  $j$  refer to the energy bins, and  $N_j^X$  stands for the number of events at the bin  $j$  for the interaction type  $X$ , computed as in Eq. (16) (i.e., with no detector effects). Note that, barring the boundary effects, the smearing produced by the migration matrices does not have an impact on the total number of events. Our full set of migration matrices, calculated for the energies up to 8 GeV using 0.1 GeV bins, and the cross sections is available at [67].

In our oscillation analysis described Sec. VI, the migration matrices are always used to account for the effect of the detector properties on the neutrino-event distributions. However, it is illustrative to compare the effective neutrino-energy resolution obtained from our realistic estimates to the values usually assumed in phenomenological oscillation studies, as shown in Fig. 5 for both the calorimetric (upper panel) and kinematic (lower panel) methods. In both cases, the bands show the range of values obtained for the standard deviation of the PDFs obtained from our Monte Carlo simulation, as a function of the neutrino energy. The lower edge of each band corresponds to the results using the setup labeled as “perfect reconstruction”, while the upper edge of the band corresponds to the setup labeled as “realistic” (see Sec. IV for details). Results are shown for QE events (darker bands) and DIS events (lighter bands). A few examples of simple functions of the neutrino energy are also shown as black lines for comparison. For reference, the values of typically used in phenomenological studies for setups using liquid argon (such as DUNE or LBNO) or totally active scintillator detectors (such as NO $\nu$ A) are typically assumed to be in the ballpark of  $\sigma(E_\nu) \sim \mathcal{O}(0.05 - 0.2)\sqrt{E_\nu}$ , see for instance Refs. [57, 63–66, 68]. The values used to simulate Cherenkov detectors in phenomenological studies (such as T2K), on the other hand, are usually in the range of  $\sigma(E_\nu) \sim \mathcal{O}(0.08)\sqrt{E_\nu}$ , see for instance Refs. [65, 69].

Finally, Fig. 6 shows the mode of the distributions as a function of the true value of the neutrino energy. The bands show our results as obtained from the Monte Carlo simulation, while the lines show the expected results in the case when the energy is perfectly reconstructed ( $E_{\text{rec,mode}} = E_{\text{true}}$ ) as well as when the neutrino energy is underestimated by 10% and by 20%. Again in this case, upper and lower panels correspond to calorimetric and kinematic reconstruction methods, respectively. The mode for QE events turns out to be in very good agreement with the true energy, regardless of the reconstruction method (see also Fig. 4). Although in the QE case, the band’s width is very small, due to small im-



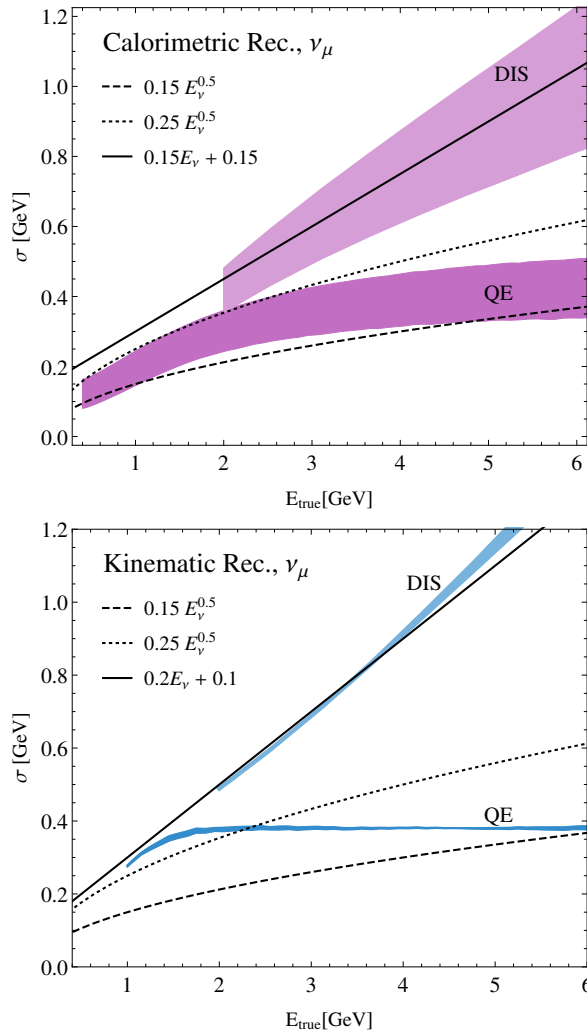


FIG. 5. (color online). Effective resolution for the neutrino energy as a function of the true energy in GeV. The bands show the standard deviation of the distribution obtained in our simulations with Monte Carlo data: the upper (lower) edge corresponds to a detector with realistic (perfect) reconstruction capabilities, as described in Sec. IV. Darker (lighter) bands correspond to the results obtained for QE (DIS) events. For comparison, a few simple examples for neutrino smearing functions frequently used in phenomenological oscillation studies are also shown.

part of the detector effects, it should be noted that the distributions are generally asymmetric, with a longer tail towards lower energies, as shown in Fig. 4.

On the other hand, for DIS events, the neutrino energy can be underestimated by up to a 20% in the case of calorimetric reconstruction, and by a much larger amount in the case of kinematic reconstruction. In the calorimetric case, this is due to the energy carried away by unobserved particles in the event. In the kinematic case, on the other hand, the main reason is that its underlying approximations are generally not satisfied for DIS events,

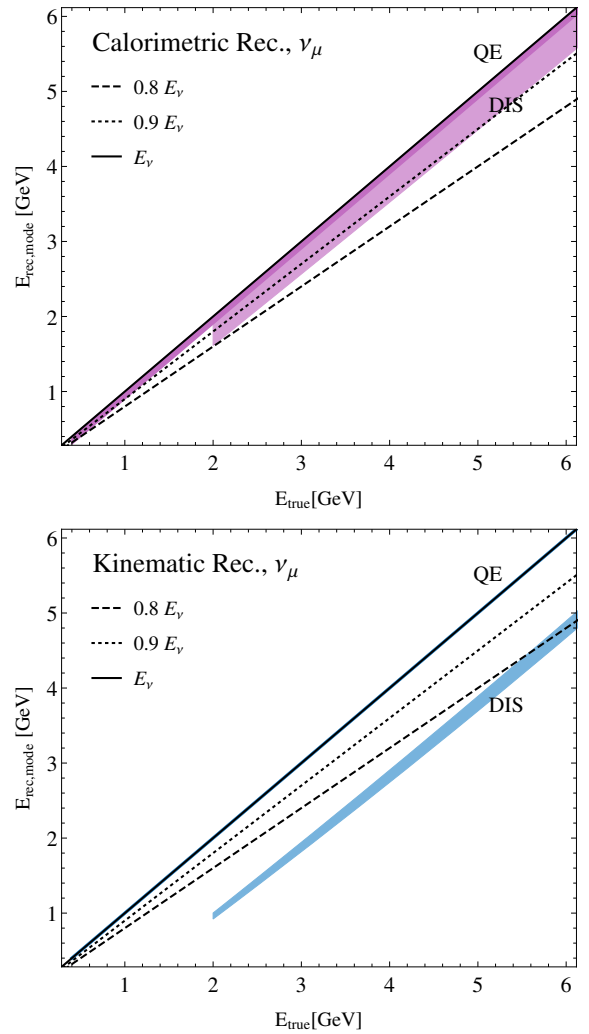


FIG. 6. (color online). Mode of the reconstructed-energy distributions as a function of the true neutrino energy. The bands show the mean of the distribution obtained in our simulations with Monte Carlo data: the lower edge corresponds to a detector with perfect reconstruction capabilities, while the upper edge corresponds to a “realistic” detector, see Sec. IV. Darker (lighter) bands correspond to the results obtained for QE (DIS) events. For comparison, the different lines show the expected result when the energy is approximately reconstructed around the true value, as well as when it is underestimated (on average) by a 10% and a 20%.

see Sec. II.

The results shown in Figs. 5 and 6 clearly show that in the kinematic method, the bands are very narrow. This means that the angular and momentum resolutions assumed for muon allow very accurate predictions for the effective resolution in terms of the neutrino energy. In the calorimetric case, on the other hand, the realistic detection capabilities for different hadrons involved in events have a more significant impact on the neutrino energy reconstruction process. This eventually makes it more



difficult to make a prediction for the final effective neutrino energy resolution.

## VI. OSCILLATION ANALYSIS

The expected event number in a neutrino-energy bin can in principle be computed, before considering any detector effects, as

$$N_{\beta}^i = \int_{E_{\nu}^i}^{E_{\nu}^i + \Delta E_{\nu}} dE_{\nu} \sigma_{\nu\beta}(E_{\nu}) P_{\alpha\beta}(\{\Theta\}, E_{\nu}) \phi_{\nu\alpha}(E_{\nu}). \quad (16)$$

Here, the indices  $\alpha$  and  $\beta$  label the initial and final neutrino flavors, respectively,  $\Delta E_{\nu}$  is the energy-bin size,  $\sigma_{\nu\beta}$  denotes the  $\nu_{\beta}$  cross section, and  $\phi_{\nu\alpha}$  is the unoscillated  $\nu_{\alpha}$  flux. The  $\nu_{\alpha} \rightarrow \nu_{\beta}$  oscillation probability,  $P_{\alpha\beta}$ , depends on a set of oscillation parameters  $\{\Theta\}$  as well as on the neutrino energy  $E_{\nu}$ . In the  $\nu_{\mu} \rightarrow \nu_{\mu}$  oscillation channel, the oscillation probability can be approximated as:

$$P_{\mu\mu} \simeq 1 - \sin^2 \theta_{\mu\mu} \sin^2 \left( \frac{\Delta m_{\mu\mu}^2 L}{4E_{\nu}} \right),$$

where  $\sin^2 \theta_{\mu\mu} = 4 \cos^2 \theta_{13} \sin^2 \theta_{23} (1 - \cos^2 \theta_{13} \sin^2 \theta_{23})$ , and  $\Delta m_{\mu\mu}^2$  is the weighted average of  $\Delta m_{31}^2$  and  $\Delta m_{32}^2$  [70] and can be approximated as  $\Delta m_{\mu\mu}^2 = \Delta m_{31}^2 + \mathcal{O}(\Delta m_{21}^2)$ .

Should the experimental information on the  $E_{\nu}$  distribution of events be available, the values of the oscillation parameters  $\{\Theta\}$  could be, in principle, directly inferred from the data<sup>1</sup>. However, modern neutrino beams are produced as tertiary products, originating predominantly from the decay of pions and kaons produced in interactions of protons impinging on a target. Therefore, neutrinos are not monoenergetic and, at a given event, the incident neutrino energy has to be reconstructed from the kinematics of the particles in the final state. Systematic uncertainties of this procedure inevitably depend on the capabilities of the employed detector, as well as on the neutrino interaction channel, owing to the different detection efficiencies for the particles involved in the event. As for muons, the efficiency uncertainty is minimal, its effect on the reconstructed energy spectrum is neglected in our analysis.

The kinematic method of energy reconstruction—used for instance in Cherenkov detectors—is known to be accurate to  $\sim 100$ – $150$  MeV for QE events [78]. However, as discussed in Sec. II, this is not the case for the events of QE topology containing undetected hadrons. For example, a single undetected pion typically spoils the reconstructed energy by  $\sim 300$ – $350$  MeV [36]. For pion-production events, playing an important role at higher

energies, either the accuracy is reduced [see Eq. (8) containing  $W^2$ , unknown on event-by-event basis] or detailed angular information is required [see Eq. (9)].

Phenomenological analyses for wide-band neutrino beams operating in the multi-GeV energy regime have shown that the sensitivity to neutrino oscillation parameters obtained with a Cherenkov detector or a liquid-argon detector is approximately similar, as long as the considered mass of the Cherenkov detector is  $\sim 3$ – $6$  times larger to compensate for its much lower efficiency for non-QE events [57, 79–82]. It has been argued that the reason lies in the imaging capabilities of the liquid-argon technology, able to identify proton in addition to lepton tracks [57], as opposed to Cherenkov detectors where the information on CC events comes predominantly from the charged leptons. Nevertheless, in such comparisons, the neutrino energy resolution at liquid-argon detectors was always assumed to be extremely good, in the range of  $\sigma(E_{\nu}) \sim 0.15\sqrt{E_{\nu}}$ . Should this be affected by detector effects, or by the energy carried away by unobserved particles, such conclusions may have to be re-examined.

In this work, we compare the kinematic and calorimetric methods of neutrino energy reconstruction in the context of a  $\nu_{\mu}$  disappearance experiment. Four types of CC neutrino interactions are considered—resonant and nonresonant pion production, two-nucleon knockout, and quasielastic scattering—and modeled according to GENIE with the  $\nu T$  package, as described in Sec. III. The coherent channel has not been taken into account because of its negligible contribution to the event rate [83]. For each interaction type and both reconstruction methods, we have calculated corresponding migration matrices  $\mathcal{M}_{ij}^X$  with and without detector effects, see Secs. IV and V.

In the  $\nu_{\mu} \rightarrow \nu_{\mu}$  oscillation channel, the main background comes from neutral current events misidentified as CC ones. As it is generally expected to be very low, for simplicity, we neglect it in our analysis. On the other hand, due to the large event statistics, systematic uncertainties are expected to be relevant. In their treatment, we follow that of Refs. [84, 85], with the  $\chi^2$  implementation as detailed in the Appendices of Refs. [85, 86]. A 20% bin-to-bin uncorrelated systematic uncertainty is assumed, as well as a 20% overall normalization uncertainty, which is bin-to-bin correlated. The pull method is used, adding a Gaussian prior for each systematic error, and the final  $\chi^2$  profile is obtained after minimization over the nuisance parameters. These (rather conservative) systematic uncertainties are introduced in our analysis in order to accommodate possible differences in the shape of the expected event distributions at the detectors, in a similar fashion as it was done in Refs. [84, 85]. A near detector is also considered in the analysis, which helps to constrain the nuisance parameters during the fit.

The oscillation analysis is performed using a modified version [86] of GLOBES (General Long Baseline Experiment Simulator) [87, 88]. The assumed true values of

<sup>1</sup> If more than one parameter is being determined from the data severe degeneracies among the different parameters may take place, though [71–77]

the oscillation parameters are

$$\begin{aligned} \Delta m_{21}^2 &= 7.50 \times 10^{-5} \text{ eV}^2; & \Delta m_{31}^2 &= 2.46 \times 10^{-3} \text{ eV}^2; \\ \theta_{12} &= 33.48^\circ; & \theta_{23} &= 42.30^\circ; & \theta_{13} &= 8.50^\circ; & \delta_{CP} &= 0. \end{aligned} \quad (17)$$

In the analysis, we focus on the determination of atmospheric parameters  $\theta_{23}$  and  $\Delta m_{31}^2$ . For simplicity, all oscillation parameters have been fixed during the analysis, i.e., no marginalization has been performed when obtaining the allowed confidence regions. However, our conclusions are not expected to change significantly if marginalization was performed within the currently allowed experimental regions. Matter effects are included in our simulations, and the matter density profile has been chosen according to the Preliminary Reference Earth Model (PREM) [89].

### A. Considered experimental setups

Oscillation experiments using neutrino beams produced from meson decays in flight can be divided into two main categories according to their far detector locations: on-axis (such as K2K [90] and MINOS [4], and also the DUNE [6] and LAGUNA-LBNO [91] proposals) and off-axis (for instance, ongoing T2K [1] and NO $\nu$ A [5]).

Due to the pion-decay kinematics, the flux at an off-axis site is well-localized around a given neutrino energy, with the beam spread and high-energy tail heavily reduced [92]. Such design allows for a significant reduction of the backgrounds coming from neutral-current events, and guarantees that the range of values of  $L/E_\nu$  is well-localized around the first oscillation maximum. The price to pay is a lower beam intensity compared to an on-axis configuration. The mean neutrino energy is also lower than in an on-axis experiments, which translates into a smaller number of event at the far detector since the cross section increases with increasing energy.

On the other hand, in an on-axis neutrino oscillation experiment, the spread of the beam is larger. In principle, this allows to determine the *shape* of the oscillation probability by performing measurements at different values of  $L/E_\nu$ . In addition, thanks to the higher beam intensity and higher neutrino energies, large event statistics is easier to collect. As a consequence of being more energetic, though, the event sample will generally contain a significant fraction of events containing pions. In addition, the high energy tail will typically produce a significant neutral-current background contamination in the low-energy bins.

In this article, we perform an analysis of two different neutrino oscillation experiments: a high-energy (HE) setup with a broad-band on-axis beam, and a low-energy (LE) setup with a narrow-band off-axis beam.

In the LE setup, we use the neutrino beam of Ref. [93], being a preliminary estimate of that in the T2K experiment with the 2.5° off-axis configuration [94]. As shown

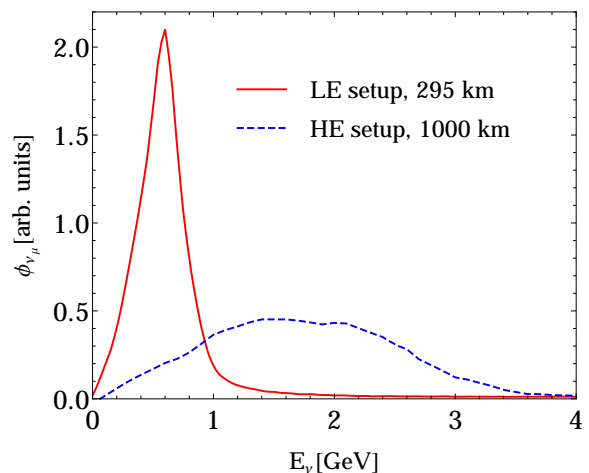


FIG. 7. (color online). The muon neutrino fluxes (in arbitrary units) for the two setups considered in this work, as a function of the neutrino energy in GeV. The solid red (dashed blue) line corresponds to the low (high) energy setup.

TABLE I. Expected number of *unoscillated* CC  $\nu_\mu$  events for the low- and high-energy setups defined in the text. In addition to the total event numbers, their breakup into different reaction mechanisms, labelled as in Fig. 1, is also given.

	QE	2p2h	res	DIS	total
LE (0.3 - 2 GeV)	47%	31%	20%	2%	5160
HE (0.3 - 4 GeV)	26%	12%	36%	26%	4549

in Fig. 7, it is peaked at around 600 MeV. As the distance to the far detector for the LE setup, we take 295 km, the distance corresponding to the first oscillation maximum. The normalization (i.e., number of protons on target, detector size, and data-taking time) have been arbitrarily set to obtain a total unoscillated CC inclusive event sample of  $\sim \mathcal{O}(5000)$  events in the energy range between 0.3 and 2 GeV, relevant for the analysis.

For the HE option, the neutrino flux labeled as “650 km” in Ref. [95] is used, corresponding to one of the configurations considered within the LAGUNA design study [96]. This flux has a broad peak between  $\sim 1$  and  $\sim 2$  GeV, with a non-negligible tail extending well above 3 GeV, see Fig. 7. We considered several choices for the distance to the far detector in the range  $L \sim \mathcal{O}(500 - 1000)$  km, for which the first oscillation maximum would lie within the energy range of the flux peak, and found  $L \sim 1000$  km to give optimal results in the  $\nu_\mu$  disappearance channel. In the following, we will show our results for this baseline choice only.

Since in this work we are only interested in exploring detector effects on different energy-reconstruction methods, the normalization for the HE setup has been arbitrarily set to obtain a similar total number of unoscillated

events as for the LE setup. However, due to the much higher neutrino energies, the composition of the inclusive event sample is very different. To illustrate this point, the total number of unoscillated CC inclusive events at the far detector are given in Table I for both setups, together with the percentages for QE, 2p2h, res and DIS events in each sample.

Finally it should be noted that, during our calculations, all neutrino events with energies between 0.2 GeV and 8 GeV are computed for both LE and HE setups. However, only those which are reconstructed between 0.3 GeV and 2 GeV (4 GeV) for the LE (HE) setup are considered during the fit. The  $\chi^2$  is built by binning the events in reconstructed neutrino energy, using 100 MeV bins.

### B. Results for the calorimetric method

As explained in Sec. II, in the calorimetric method, the neutrino energy is reconstructed by adding the energies of all observed particles in the final state and no information on the direction of the outgoing particles is used.

Our results for the calorimetric method are shown in the lower panels in Figs. 8 and 9 for the LE and HE setups, respectively, where we show the confidence regions for a fit to the atmospheric oscillation parameters in a few cases. In the fits, the *true* event rates are computed using the assumed true values of the oscillation parameters [indicated by a star and given in Eq. (17)]. This is the event distribution that we expect to be observed in a real experiment, and is therefore simulated using our realistic setup, defined in Sec. IV.

However, in an experimental analysis, one has to rely on a Monte Carlo simulation to predict the “expected” event rates, which will be referred to as “fitted” rates in the following. In the simulation certain assumptions have to be made regarding the detector performance, and they are subject to uncertainties.

Because it is computationally expensive to generate a given set of migration matrices from simulated neutrino events, in our simulations the “fitted” rates are generated using a linear combination of the matrices obtained for the realistic and perfect detection capabilities. This allows for a continuous transformation of the event-rate distribution from one scenario to another, useful to quantify when the incorrect estimation of the detector performance starts to have a significant impact on the fit. Practically, the fitted rates are obtained as:

$$N_i^{\text{fit}} = \sum_X \sum_j \left\{ (1 - \alpha) M_{ij}^{X, \text{real}} + \alpha M_{ij}^{X, \text{perf}} \right\} N_j^X, \quad (18)$$

where  $X$  stands for a given type of interaction (QE, 2p2h, res or DIS), and  $i$  and  $j$  are energy bin indices.  $M^{X, \text{real}}$  and  $M^{X, \text{perf}}$  denote the migration matrices obtained assuming realistic and perfect detection capabilities, respectively. Finally,  $N_j^X$  is the event rate in the energy

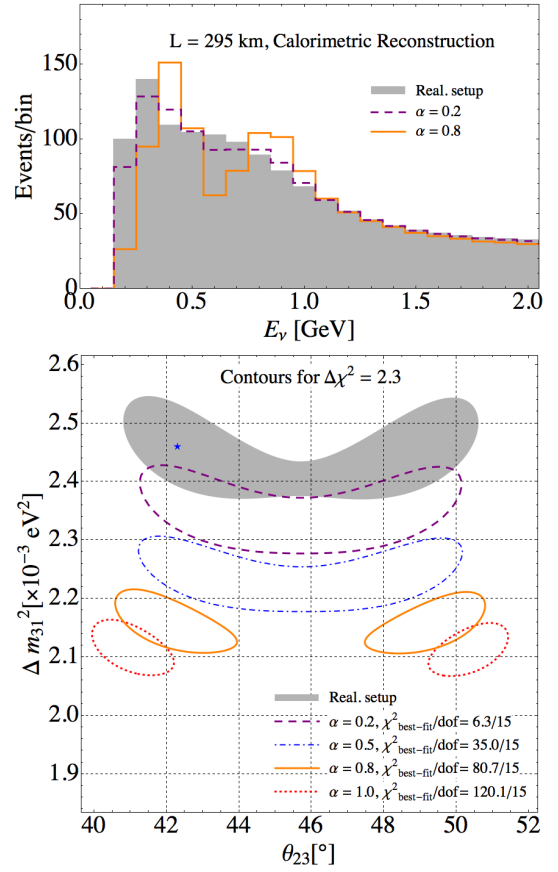


FIG. 8. (color online). Results for the low-energy setup and the calorimetric reconstruction method. Upper panel: Simulated charged-current event distributions in the far detector as a function of the reconstructed energy, for the oscillation parameters (17). The shaded histogram shows the result using the migration matrices obtained for the realistic detector setup (see Sec. IV). Dashed and solid lines show the event rates obtained if the assumptions on the detector performance are improved by a 20% and an 80% with respect to the scenario considered for the dashed histogram. Lower panel: Confidence regions in the  $(\theta_{23}, \Delta m_{31}^2)$  plane, at  $1\sigma$  CL (2 d.o.f.). The shaded areas show the regions obtained when the fit is done using the migration matrices for the realistic detector setup defined in Sec. IV. The contours shown by the colored lines are obtained if during the fit the performance of the detector is overestimated by a 20%, 50%, 80% and a 100% as indicated in the legend, see text for details. The star indicates the true values of the oscillation parameters, which is the same for all confidence regions shown.

bin  $j$  for the interaction type  $X$ , computed without accounting for the detector effects, as in Eq. (16).

In Eq. (18),  $\alpha$  is a *purely phenomenological* parameter, used to obtain the “effective” migration matrices as a linear deformation of the two extreme scenarios under consideration. For instance,  $\alpha = 0$  means that the fitted rates are obtained in the same way as the true rates. On the other hand,  $\alpha = 0.8$  means that in obtaining the fit-

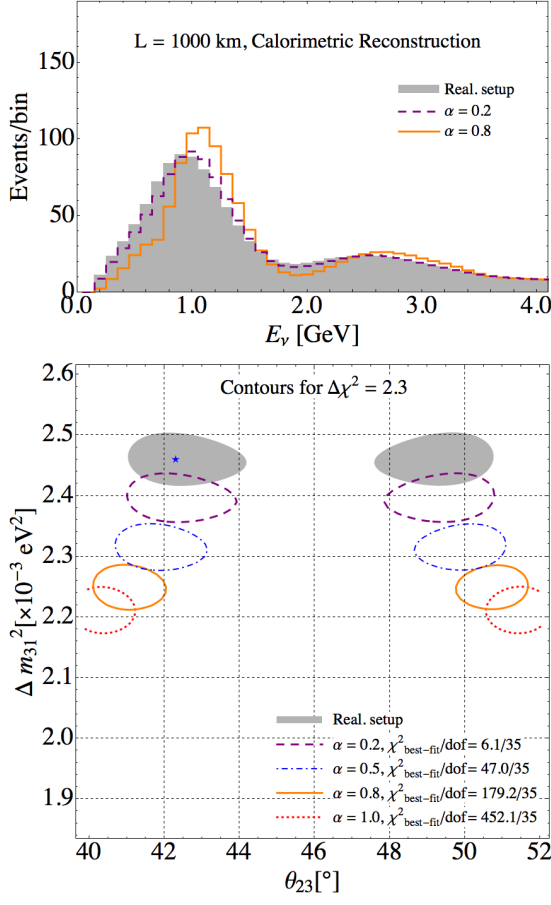


FIG. 9. (color online). Same as in Fig. 8 but for the high-energy setup and the calorimetric reconstruction method.

ted rates the detector capabilities have been incorrectly estimated by a large amount, and therefore they are more similar to the ones obtained using a detector with perfect reconstruction capabilities. A few examples for the event distributions obtained for different values of  $\alpha$  are shown in the upper panels in Figs. 8 and 9 for illustration purposes. Even though the distributions look very different, all histograms have been obtained assuming the same true values for the oscillation parameters (17).

For a given value of  $\alpha$ , the fitted rates are simulated for every possible combination of  $(\Delta m_{31}^2, \theta_{23})$ . The point in the  $(\Delta m_{31}^2, \theta_{23})$  plane which gives a best fit to the data is then identified, and the confidence regions are drawn by requiring that

$$\Delta\chi^2(\Delta m_{31}^2, \theta_{23}) \equiv \chi^2(\Delta m_{31}^2, \theta_{23}) - \chi_{\text{best-fit}}^2 < 2.30. \quad (19)$$

Since the fitted rates are generated using a different set of the migration matrices, the event distributions generally have a different shape than the true rates, and the best fit to the data does not necessarily coincide with the true values of oscillation parameters realized in Nature. This is shown in the lower panels in Figs. 8 and 9, where one

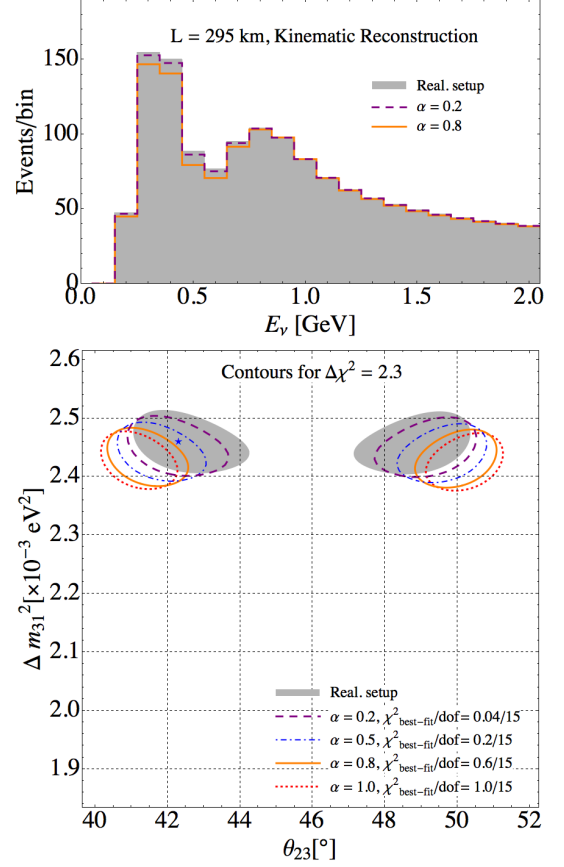


FIG. 10. (color online). Same as in Fig. 8 but using the kinematic method to reconstruct the neutrino energy.

can observe that, as the detector capabilities are incorrectly estimated, the allowed confidence regions start to drift away from the shaded areas. The minimum value of the  $\chi^2$  obtained for each value of  $\alpha$  is indicated in the legend, together with the effective number of degrees of freedom (d.o.f.) in the fit<sup>2</sup>. For  $\alpha = 0$  the value of the  $\chi^2$  at the best-fit point is negligible and therefore is not indicated in the legend.

<sup>2</sup> In our case, this corresponds to the number of bins used in the fit, minus the number of parameters determined from the data. This is typically used as a test of the validity of the model used to fit the data. In a real experiment, the minimum  $\chi^2$  would receive contributions from statistical fluctuations of the measured quantities in each data bin. If the model used to fit the data is correct, the ratio  $\chi_{\text{min}}^2/N_{\text{d.o.f.}}$  should be close to 1. In our case, no statistical fluctuations are considered in the fit. Nevertheless, the use of a wrong model when fitting the data can give a sizeable contribution to the value of  $\chi_{\text{min}}^2/N_{\text{d.o.f.}}$ . This can be estimated in our calculations as  $\chi_{\text{best-fit}}^2/N_{\text{d.o.f.}}$ .

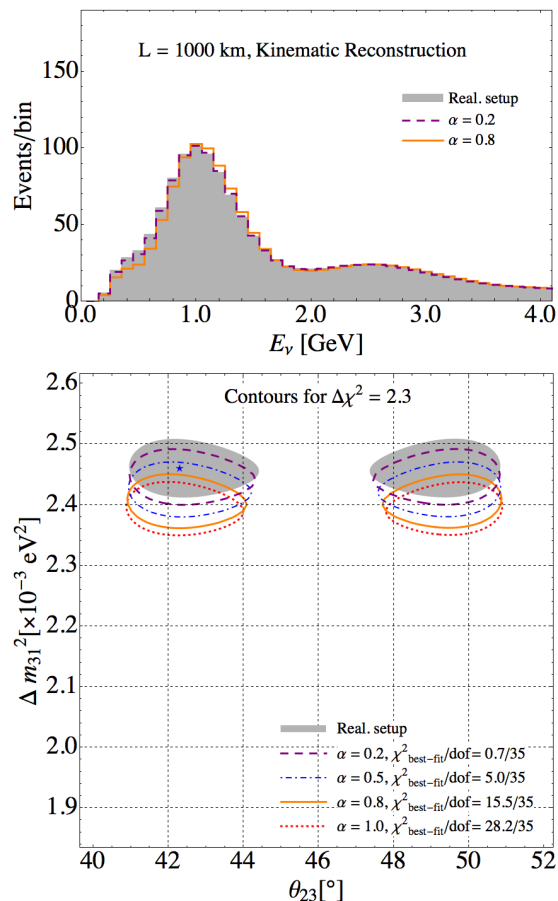


FIG. 11. (color online). Same as in Fig. 8 but for the high energy setup and the kinematic energy reconstruction.

### C. Results for the kinematic method

In the kinematic method, the neutrino energy is reconstructed using only the direction and momentum of the outgoing charged lepton (in our case, a muon) in the final state, and no kinematic information from the outgoing hadrons in the final state is needed.

As in Sec. VIB, the true event distribution is computed using the migration matrices accounting for realistic detection capabilities, while the fitted rates are computed following Eq. (18), and the confidence regions satisfy Eq. (19).

Our results for the kinematic reconstruction method are shown in Figs. 10 and 11 for the LE and HE setups, respectively. For the shaded areas, the true and fitted rates are generated using the same set of migration matrices and therefore the best fit coincides with the true values. However, as in the case of calorimetric reconstruction, when the value of  $\alpha$  is increased the confidence regions start to drift away from the shaded areas. The reason for this is that, for non-zero values of  $\alpha$ , the shapes of the event distributions are generally different

from that of the true rates (even for the same value oscillation probability) and the best-fit for the oscillation parameters will no longer coincide with the true values.

However, it should be noted that in this case the effect of the mismatch between the actual and assumed detector capabilities is much milder than for the calorimetric method. The confidence regions show a significant overlap, even for the extreme case  $\alpha = 1$ , when the detector performance is assumed to be perfect in the data fit. The main reason for this is that the muon reconstruction is very precise in modern detectors, while for electrons and hadrons this is more difficult to achieve (see also Figs. 5 and 6). It should be noted, however, that in this study we assume that the muon track is fully contained in the detector, regardless of its energy. Should this assumption be relaxed, the muon momentum determination may be affected and, as a consequence, also the neutrino energy reconstruction.

## VII. SUMMARY

It has been realized for a while now that an accurate understanding of neutrino-nucleus scattering is an essential ingredient for accelerator-based neutrino-oscillation experiments. More recently, quantitative studies have tackled the relation between uncertainties in cross-section modeling and the resulting physics sensitivities for oscillation measurements. For example, it was shown that for quasielastic events, energy reconstruction based purely on the kinematic observables of the outgoing lepton is susceptible to a large bias resulting from the underlying nuclear-interaction model [84, 85]. In this article, we fully rely on the nuclear model used for event generation, and have a critical look at the impact of realistic detector effects.

From energy conservation, it is clear that a perfect calorimeter—i.e., a detector able to measure the total energy of all reaction products—would be free from any bias in energy reconstruction [97]. In this article we aim at quantifying how close to the perfect scenario the calorimetric energy reconstruction is, when finite energy resolutions, detection efficiencies, and thresholds are accounted for. In addition, we compare the role of realistic detection capabilities on the calorimetric and kinematic analysis. In the latter case, we use—although in a simplistic way—the information on that the charged lepton’s kinematics also for non-QE events.

In a nutshell, we find that kinematic reconstruction is very robust with respect to detector effects, largely because muons are the most precisely reconstructed particles in modern neutrino detectors. On the other hand, the actual performance of a calorimetric analysis clearly depends on the assumption made about detector performance. The chosen detection capabilities are not meant to represent any existing detector, but are indicative of the general level of performance which can be expected. To translate these result for a specific experiment, a de-

tailed study of detector response—beyond the scope of this work—is required. Many of the analysis techniques developed here, however should turn out to be very useful. Interestingly, we find the kinematic analysis performs well even for pion-production events but independence of this observation from the underlying nuclear model is to be examined.

We limit this study to the  $\nu_\mu$  disappearance channel since this can be effectively treated as a two-flavor oscillation and the effect of energy resolution and energy-reconstruction bias are directly related to the precision on the  $\Delta m^2$  and a shift of the value of  $\Delta m^2$ , respectively. We use a phenomenological parametrization to interpolate between a perfect and realistic detector. This allows us to conclude that, overall, the detector response—in terms of efficiencies, resolutions, and thresholds for individual particles—has to be understood at a 10% level or better to avoid a significant bias in the measurement of  $\Delta m^2$ . For the kinematic analysis these requirements are much less stringent, but uncertainties of the nuclear model, not considered here, present a challenge, as shown previously in the literature.

In summary, while the calorimetric reconstruction may be less sensitive to the underlying nuclear model, it is strongly affected by detector effects, typically leading to

energy underestimation. On the other hand, the kinematic method of neutrino energy reconstruction is much less challenging for the detector design but it strongly relies on an accurate understanding of neutrino-nucleus interactions. One needs to keep in mind that the quantitative details of our conclusions may be specific to this work, owing to the underlying detector assumptions. However, their qualitative aspects can be expected to hold for a variety of experiments.

## ACKNOWLEDGMENTS

The work of AMA, CMJ, and CM was supported by the National Science Foundation under Grant No. PHY-1352106. Fermilab is operated by the Fermi Research Alliance under contract no. DE-AC02-07CH11359 with the U.S. Department of Energy. PC acknowledges partial support from the European Union FP7 ITN INVISIBLES (Marie Curie Actions, PITN- GA-2011- 289442). PH is supported by the U.S. Department of Energy under contract DE-SC0013632. The work of DM and EV was supported by MIUR (Italy) under the program “Futuro in Ricerca 2010 (RBFR100360)”. EV acknowledges the hospitality and support from Center for Neutrino Physics of Virginia Tech.

- 
- [1] K. Abe *et al.* (T2K Collaboration), Nucl. Instrum. Methods Phys. Res., Sect. A **659**, 106 (2011).
  - [2] A. A. Aguilar-Arévalo *et al.* (MiniBooNE Collaboration), Nucl. Instrum. Methods Phys. Res., Sect. A **599**, 28 (2009).
  - [3] M. Martini, M. Ericson, G. Chanfray, and J. Marteau, Phys. Rev. C **80**, 065501 (2009).
  - [4] D. G. Michael *et al.* (MINOS Collaboration), Nucl. Instrum. Methods Phys. Res., Sect. A **596**, 190 (2008).
  - [5] D. S. Ayres *et al.* (NO $\nu$ A Collaboration), Fermilab-Proposal-0929, arXiv:hep-ex/0503053.
  - [6] C. Adams *et al.* (LBNE Collaboration), arXiv:1307.7335.
  - [7] H. Gallagher, talk given at the INT Workshop “Neutrino-Nucleus Interactions for Current and Next Generation Neutrino Oscillation Experiments” (INT-13-54W), Seattle, USA, 3–13 December 2013; the slides and video available at [http://www.int.washington.edu/talks/WorkShops/int\\_13\\_54W/](http://www.int.washington.edu/talks/WorkShops/int_13_54W/).
  - [8] Q. Wu *et al.* (NOMAD Collaboration), Phys. Lett. **B660**, 19 (2008).
  - [9] V. V. Lyubushkin *et al.* (NOMAD Collaboration), Eur. Phys. J. C **63**, 355 (2009).
  - [10] A. A. Aguilar-Arévalo *et al.* (MiniBooNE Collaboration), Phys. Rev. D **81**, 092005 (2010).
  - [11] A. A. Aguilar-Arévalo *et al.* (MiniBooNE Collaboration), Phys. Rev. D **82**, 092005 (2010).
  - [12] A. A. Aguilar-Arévalo *et al.* (MiniBooNE Collaboration), Phys. Rev. D **83**, 052007 (2011).
  - [13] A. A. Aguilar-Arévalo *et al.* (MiniBooNE Collaboration), Phys. Rev. D **83**, 052009 (2011).
  - [14] Y. Nakajima *et al.* (SciBooNE Collaboration), Phys. Rev. D **83**, 012005 (2011).
  - [15] L. Fields *et al.* (MINERvA Collaboration), Phys. Rev. Lett. **111**, 022501 (2013).
  - [16] G. A. Fiorentini *et al.* (MINERvA Collaboration), Phys. Rev. Lett. **111**, 022502 (2013).
  - [17] K. Abe *et al.* (T2K Collaboration), Phys. Rev. D **87**, 092003 (2013).
  - [18] A. A. Aguilar-Arévalo *et al.* (MiniBooNE Collaboration), Phys. Rev. D **88**, 032001 (2013).
  - [19] K. Abe *et al.* (T2K Collaboration), Phys. Rev. D **90**, 052010 (2014).
  - [20] B. G. Tice *et al.* (MINERvA Collaboration), Phys. Rev. Lett. **112**, 231801 (2014).
  - [21] K. Abe *et al.* (T2K Collaboration), Phys. Rev. Lett. **113**, 241803 (2014).
  - [22] A. Higuera *et al.* (MINERvA Collaboration), Phys. Rev. Lett. **113**, 261802 (2014).
  - [23] A. A. Aguilar-Arévalo *et al.* (MiniBooNE Collaboration), Phys. Rev. D **91**, 012004 (2015).
  - [24] T. Walton *et al.* (MINERvA Collaboration), Phys. Rev. D **91**, 071301(R) (2015).
  - [25] K. Abe *et al.* (T2K Collaboration), Phys. Rev. D **91**, 112002 (2015).
  - [26] B. Eberly *et al.* (MINERvA Collaboration), arXiv:1406.6415.
  - [27] K. Abe *et al.* (T2K Collaboration), arXiv:1411.6264.
  - [28] L. Aliaga *et al.* (MINERvA Collaboration), arXiv:1503.02107.
  - [29] C. Andreopoulos *et al.*, Nucl. Instrum. Methods Phys. Res., Sect. A **614**, 87 (2010).



- [30] C.-M. Jen, A. M. Ankowski, O. Benhar, A. P. Furmanski, L. N. Kalousis, and C. Mariani, Phys. Rev. D **90**, 093004 (2014).
- [31] O. Benhar, A. Fabrocini, S. Fantoni, and I. Sick, Nucl. Phys. **A579**, 493 (1994).
- [32] D. G. Michael *et al.* (MINOS Collaboration), Phys. Rev. Lett. **97**, 191801 (2006).
- [33] O. Benhar and D. Meloni, Phys. Rev. D **80**, 073003 (2009).
- [34] M. H. Ahn *et al.* (K2K Collaboration), Phys. Rev. Lett. **90**, 041801 (2003).
- [35] A. A. Aguilar-Arévalo *et al.* (MiniBooNE Collaboration), Phys. Rev. Lett. **100**, 032301 (2008).
- [36] T. Leitner and U. Mosel, Phys. Rev. C **81**, 064614 (2010).
- [37] M. Martini, M. Ericson, and G. Chanfray, Phys. Rev. D **85**, 093012 (2012).
- [38] M. Martini, M. Ericson, and G. Chanfray, Phys. Rev. D **87**, 013009 (2013).
- [39] O. Lalakulich, K. Gallmeister, and U. Mosel, Phys. Rev. C **86**, 014614 (2012).
- [40] S. Dytman, in *12th International Workshop on Neutrino Factories, Superbeams, and Betabeams (NuFact10) (Mumbai, India, 2010)*, edited by B. S. Acharya, M. Goodman, and N. K. Mondal, AIP Conf. Proc. No. 1382 (AIP, New York, 2011), p. 156.
- [41] D. Rein and L. M. Sehgal, Ann. Phys. (N.Y.) **133**, 79 (1981).
- [42] A. Bodek and U.-K. Yang, J. Phys. G **29**, 1899 (2003).
- [43] A. Bodek, I. Park, and U.-K. Yang, Nucl. Phys. B, Proc. Suppl. **139**, 113 (2005).
- [44] T. Yang, C. Andreopoulos, H. Gallagher, K. Hofmann, and P. Kehayias, Eur. Phys. J. C **63**, 1 (2009).
- [45] Z. Koba, H.B. Nielsen, and P. Olesen, Nucl. Phys. **B40**, 317 (1972).
- [46] T. Sjöstrand, S. Mrenna, and P. Skands, J. High Energy Phys. **05** (2006) 026.
- [47] T. Katori, in *NuInt12: The 8th International Workshop on Neutrino-Nucleus Interactions in the Few-GeV Region*, edited by Hélio da Motta, Jorge G. Morfin, and Makoto Sakuda, AIP Conf. Proc. **1663**, 030001 (2015).
- [48] J. W. Lightbody Jr. and J. S. O'Connell, Comput. Phys. **2**, 57 (1988).
- [49] C. H. Llewellyn Smith, Phys. Rep. **3**, 261 (1972).
- [50] A. Bodek and J. L. Ritchie, Phys. Rev. D **23**, 1070 (1981).
- [51] O. Benhar, D. Day, and I. Sick, Rev. Mod. Phys. **80**, 189 (2008).
- [52] O. Benhar, A. Fabrocini, and S. Fantoni, Nucl. Phys. **A505**, 267 (1989).
- [53] J. Mougey *et al.*, Nucl. Phys. **A262**, 461 (1976).
- [54] D. Dutta *et al.*, Phys. Rev. C **68**, 064603 (2003).
- [55] A. M. Ankowski, O. Benhar, and M. Sakuda, Phys. Rev. D **91**, 033005 (2015).
- [56] D. Rohe *et al.* (JLAB E97-006 Collaboration), Phys. Rev. C **72**, 054602 (2005).
- [57] V. Barger *et al.*, arXiv:0705.4396 [hep-ph].
- [58] S. Short, Ph.D. thesis, Imperial College London, 2013.
- [59] B. Eberly, in *NuInt12: The 8th International Workshop on Neutrino-Nucleus Interactions in the Few-GeV Region*, edited by Hélio da Motta, Jorge G. Morfin, and Makoto Sakuda, AIP Conf. Proc. **1663**, 070006 (2015).
- [60] L. Aliaga *et al.* (MINERvA Collaboration), Nucl. Instrum. Methods Phys. Res., Sect. A **743**, 130 (2014).
- [61] A. A. Aguilar-Arévalo *et al.* (MiniBooNE Collaboration), Phys. Rev. Lett. **98**, 231801 (2007).
- [62] A. Stahl *et al.*, CERN-SPSC-2012-021, SPSC-EOI-007. <http://inspirehep.net/record/1194418/files/SPSC-EOI-007.pdf>
- [63] C. Adams *et al.* (LBNE Collaboration), arXiv:1307.7335.
- [64] S. K. Agarwalla, S. Prakash, S. K. Raut, and S. U. Sankar, JHEP **1212**, 075 (2012) [arXiv:1208.3644 [hep-ph]].
- [65] S. K. Agarwalla, S. Prakash, and W. Wang, arXiv:1312.1477.
- [66] S. K. Agarwalla, T. Li and A. Rubbia, JHEP **1205**, 154 (2012) [arXiv:1109.6526 [hep-ph]].
- [67] For the migration matrices and the cross sections employed in our analysis see Supplemental Material accompanying this article. They are also available at <http://chimera.roma1.infn.it/OMAR/Erica/>.
- [68] R. B. Patterson, Nucl. Phys. B, Proc. Suppl. **235-236**, 151 (2013).
- [69] P. Huber, M. Lindner, T. Schwetz, and W. Winter, JHEP **0911**, 044 (2009) [arXiv:0907.1896 [hep-ph]].
- [70] H. Nunokawa, S. J. Parke, and R. Zukanovich Funchal, Phys. Rev. D **72**, 013009 (2005).
- [71] G. L. Fogli and E. Lisi, Phys. Rev. D **54**, 3667 (1996).
- [72] V. Barger, D. Marfatia, and K. Whisnant, Phys. Rev. D **65**, 073023 (2002).
- [73] J. Burguet-Castell, M. B. Gavela, J. J. Gomez-Cadenas, P. Hernandez, and O. Mena, Nucl. Phys. **B608**, 301 (2001).
- [74] H. Minakata and H. Nunokawa, JHEP **0110**, 001 (2001) [hep-ph/0108085].
- [75] A. Donini, D. Meloni, and S. Rigolin, JHEP **0406** (2004) 011 [hep-ph/0312072].
- [76] H. Minakata and S. J. Parke, Phys. Rev. D **87**, 113005 (2013).
- [77] P. Coloma, H. Minakata, and S. J. Parke, Phys. Rev. D **90**, 093003 (2014).
- [78] A. M. Ankowski, Proc. Sci. NUFACT2014 (2015) 004.
- [79] P. Coloma, E. Fernandez-Martinez, and L. Labarga, JHEP **1211**, 069 (2012) [arXiv:1206.0475 [hep-ph]].
- [80] P. Coloma, T. Li, and S. Pascoli, arXiv:1206.4038 [hep-ph].
- [81] P. Huber and J. Kopp, JHEP **1103**, 013 (2011) [JHEP **1105**, 024 (2011)] [arXiv:1010.3706 [hep-ph]].
- [82] T. Akiri *et al.* (LBNE Collaboration), arXiv:1110.6249.
- [83] J. A. Formaggio and G. P. Zeller, Rev. Mod. Phys. **84**, 1307 (2012).
- [84] P. Coloma and P. Huber, Phys. Rev. Lett. **111**, 221802 (2013).
- [85] P. Coloma, P. Huber, C.-M. Jen, and C. Mariani, Phys. Rev. D **89**, 073015 (2014).
- [86] P. Coloma, P. Huber, J. Kopp, and W. Winter, Phys. Rev. D **87**, 033004 (2013).
- [87] P. Huber, M. Lindner, and W. Winter, Comput. Phys. Commun. **167**, 195 (2005).
- [88] P. Huber, J. Kopp, and M. Lindner, Comput. Phys. Commun. **177**, 432 (2007).
- [89] A. M. Dziewonski and D. L. Anderson, Phys. Earth Planet. Inter. **25**, 297 (1981).
- [90] R. Gran *et al.* (K2K Collaboration), Phys. Rev. D **74**, 052002 (2006).
- [91] S. K. Agarwalla *et al.* (LAGUNA-LBNO Collaboration), arXiv:1412.0804.
- [92] D. Beavis *et al.* (E889 Collaboration), Physics Design Report, BNL 52459, 1995; J.-M. Levy, arXiv:1005.0574.



- [93] P. Huber, M. Lindner, T. Schwetz, and W. Winter, J. High Energy Phys. **11** (2009) 044.
- [94] K. Abe *et al.* (T2K Collaboration), Phys. Rev. D **87**, 012001 (2013).
- [95] A. Longhin, [arXiv:1206.4294](#).
- [96] D. Angus *et al.* (LAGUNA Collaboration), [arXiv:1001.0077](#).
- [97] U. Mosel, [arXiv:1504.08204](#).